Ferroelectricity and piezoelectricity in elemental α-X6 structure

Xuanlin Zhang,[1,2] Luqi Dong,[2] and Yunhao Lu[2,1]
[1] *State Key Laboratory of Silicon and Advanced Semiconductor Materials, School of Materials Science and Engineering, Zhejiang University, Hangzhou 310027, China*
[2] *School of Physics, Zhejiang University, Hangzhou 310027, China*

(Received 19 April 2024; revised 17 June 2024; accepted 19 July 2024; published 2 August 2024)

Two-dimensional (2D) elemental ferroelectricity has recently been confirmed and arouses great interest in exploring new elemental asymmetric structures and their symmetry-breaking related properties. In this study, our density functional theory (DFT) calculations reveal the existence of coupled in-plane and out-of-plane electric polarizations in the group V elements α-$X6$ (X = P, As). These ferroelectric phases are stabilized through charge transfer between p_x orbitals. The introduction of compressive strain facilitates the transformation from blue phosphorene into α-P6 phase with low reaction energy owing to their structural similarity. In addition, strain engineering or atom substitution can effectively reduce the polarization switching barrier. Furthermore, α-$X6$ structure exhibits large longitudinal piezoelectric strain coefficients d_{11}, benefiting from their moderate e_{11} and flexible character. This discovery not only enriches the family of elemental ferroelectrics but also deepens the understanding of the origin of elemental polarization, offering potential candidates for ferroelectric and piezoelectric applications.

DOI: 10.1103/PhysRevMaterials.8.084401

I. INTRODUCTION

The polarization in ferroelectrics is usually caused by the spatial separation of cations and anions without inversion symmetry. Conventionally, elemental materials seem to have no electronegative distinction between atoms and remain nonpolar structures of high symmetry. The first prediction of elemental ferroelectricity was group-V element α-(As, Sb, Bi), where charge transfer between sublattice produces lone pairs on the p_z orbital and causes the buckled polar structure with in-plane polarization [1]. Recently, this ferroelectricity of monolayer α-Bi has been confirmed experimentally [2].

Inspired by this counterintuitive finding, researches are under taken to explore the ferroelectric behavior of 2D elemental layers. Ferroelectricity has been proposed in 2D penta-Silicene [3] and the Silicon(001) surface [4]. Several quasi-2D structures of group-VI elements also exhibit in-plane ferroelectricity [5,6]. Based on the sliding ferroelectric theory, out-of-plane polarizations have been discovered in graphite [7,8] and blue phosphorous [9] with specific stacking. Notably, these elemental structures show a remarkable longitudinal piezoelectric effect [10,11] and anomalous negative piezoelectric properties [12,13], holding significant promise for practical applications. In addition, their symmetry-breaking associated nonlinear optical responses [13,14] and bulk photovoltaic effects [15] are also under investigation.

As an element with five valence electrons, group-V elemental materials have abundant allotropes that have been theoretically predicted and experimentally synthesized [16–22]. For example, there are black and blue phosphorene showing excellent properties that are promising for next-generation electronics [23–25]. However, both of them are inherently centrosymmetric without polar structures. Different from the perfect 2D structures, surfaces and interfaces break symmetry and could introduce noncentrosymmetric structures. Some polar structures have already been predicted at the boundary between blue phosphorene domains, possibly exhibiting ferroelectric properties [26].

Here, based on DFT calculations, a novel ferroelectric structure is confirmed in group-V elements (named as α-$X6$ with X = P, As) possessing coupled in-plane and out-of-plane electric polarizations. Charge transfer and the formation of lone pair electrons lower the energy in the ferroelectric phase, constituting a crucial electronic contribution to polarization. By applying compressive strain, blue phosphorene potentially transforms into α-P6 rather than black phosphorene, as the kinetic process plays a pivotal role in this transformation. Meanwhile, strain engineering and atom substitution can decrease the polarization switching barriers. Given their moderate e_{11} value and soft character, the longitudinal piezoelectric constants d_{11} of α-$X6$ are large for electrical-mechanical energy conversion. Our discovery of α-$X6$ materials not only expands the family of elemental ferroelectrics but also enhances the understanding of the mechanisms in elemental polarization, potentially paving the way for ferroelectric and piezoelectric applications.

II. COMPUTATIONAL TECHNIQUES

The first principles calculations were performed via the Vienna *ab initio* Simulation Package (VASP) adopting the local-density approximation (LDA) for exchange-correlation functional with projector augmented-wave method [27–29]. HSE06 functional based on generalized gradient approximation structure is also applied to compare with LDA functionals [30]. The energy cutoff is set as 500 eV. A Γ-centered k-point grid of 7 × 15 × 1 was applied for sampling the Brillouin Zone. The energy and force threshold for structural optimiza-

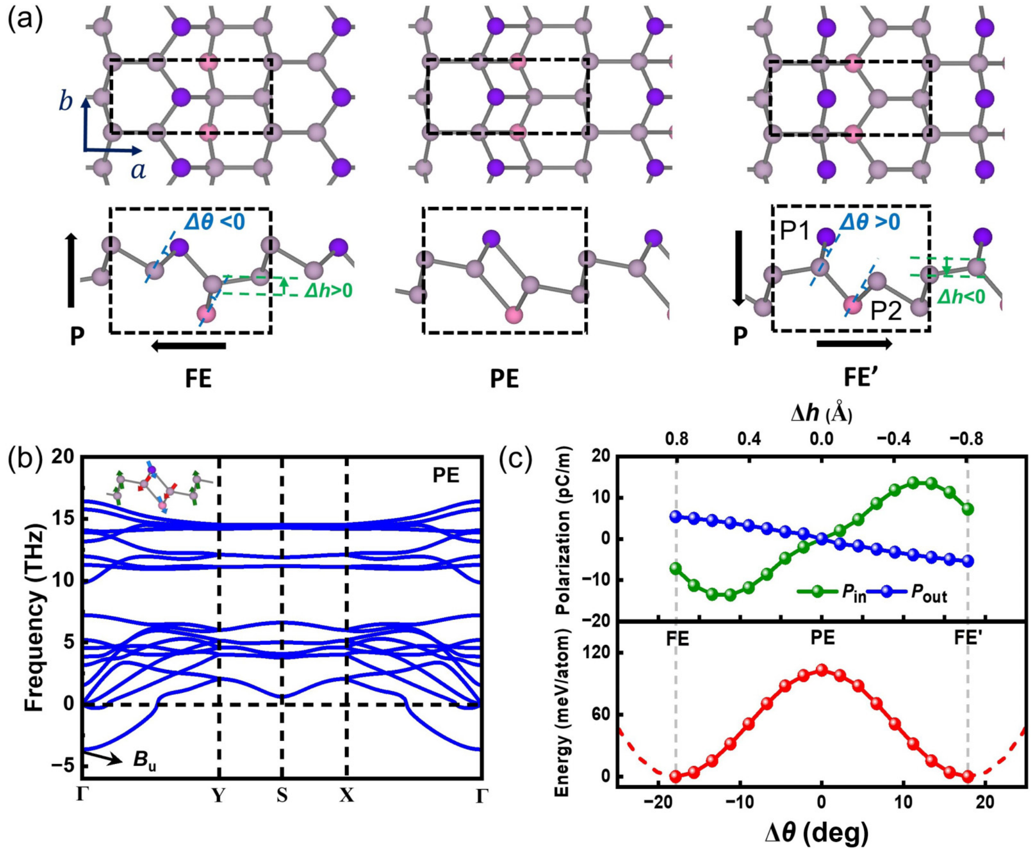

FIG. 1. (a) The top views and side views of ferroelectric (FE and FE′) and paraelectric (PE) α-P6. The black arrows denote the polarization. The purple atoms and pink atoms in the FE′ phase are labeled as P1 and P2 atoms, respectively. (b) The phonon spectrum of α-P6 PE phase with inset of the B_u phonon eigenvectors. (c) The distortion-polarization curve (green and blue circle) and distortion-energy curve (red circle) of α-P6.

tion are 10^{-6} eV and 0.005 eV/Å. A 20 Å vacuum is set to avoid periodic interactions along the c direction. The polarizations are calculated by the berry phase implemented in VASP [31]. The density functional perturbation theory (DFPT) is applied to calculate the piezoelectric and elastic properties [32]. The phase transition process is calculated by climbing image nudge elastic band (CI-NEB) methods [33]. The Scanning Tunneling Microscopy (STM) simulation is generated with VASPKIT code [34].

III. RESULTS AND DISCUSSION

As depicted in Fig. 1(a), the 2D α-X6 structure comprises six atoms within a primitive unit cell and belongs to polar Pm space group. Four atoms are three-coordinated, typical sp^3 hybridization in group V atoms. The remaining two atoms possess less common coordination numbers: two and four, respectively, which is crucial for the emergence of polarization. Since ferroelectric phase transition is usually connected with the softened optical modes in undistorted structures below Curie temperature [35], we construct a centrosymmetric paraelectric phase as a reference in the middle column of Fig. 1(a), consisting of a four-atom ring and an X-X dimer with the space group of $P2_1m$. In Fig. 1(b), we plot the phonon spectrum of the paraelectric α-P6. One observes that a soft optical mode emerges at the center of the Brillouin. From an analysis of the phonon eigenvector at the Γ point, this mode has an irreducible representation of B_u and is associated with asymmetric displacements of all six atoms as shown in the inset of Fig. 1(b). With the B_u displacement, the paraelectric phase distorts into the ferroelectric α-P6 phase without any soft mode across the Brillouin zone in its phonon spectrum as shown in Fig. S1 of the Supplemental Material [36].

The distortions of the α-P6 can be understood as the upper and lower P-P bonds in the four-atom ring rotating in opposite directions by an angle of $\Delta\theta = 17.88^\circ$, while the P-P dimer translates along the out-of-plane direction by $\Delta h = -0.81$ Å. This distortion breaks the inversion symmetry, giving rise to coupled in-plane (7.21 pC/m) and out-of-plane (5.38 pC/m) polarization as in Fig. 1(c), which is higher than that of experimentally observed double-layer ferroelectric BN (2.08 pC/m) [37–40]. Furthermore, the distortion-energy curve exhibits a typical ferroelectric double-well shape as the bottom panel in Fig. 1(c), and the CI-NEB energy curve shows a switching barrier of 55 meV/atom (Fig. S2) [36]. Meanwhile, a dynamically stable ferroelectric semiconductor α-As6 can also be obtained with distortion amplitudes of $\Delta\theta = 15.01^\circ$ and $\Delta h = -0.85$ Å as in Table I and Fig. S3 [36].

It is noteworthy that the in-plane polarization of α-P6 exhibits a nonmonotonic relationship with distortions as shown in the upper panel of Fig. 1(c), analogous to the coupled electronic and phononic ferroelectric behavior observed in

TABLE I. The structure parameters, polarizations (in unit of pC/m), and band gap of α-X6 (X = P, As).

Structure	a(Å)	b(Å)	$\Delta\theta$(°)	Δh(Å)	P_{in}	P_{out}	E_{gap}(eV)
α-P6	7.16	3.21	17.88	0.81	7.21	5.38	0.78
α-As6	7.90	3.52	15.01	0.85	34.08	6.02	0.44

previously reported h-NbN system [41]. The electronic structure of α-P6 is shown in Fig. 2(a). In the centrosymmetric states, the two P atoms (labeled as dark purple and pink) are equivalent with their p_x orbitals degenerated in energy. When the ferroelectric distortions occur, the degeneracy is lifted and the two p_x orbitals split, as schematically depicted in Fig. 2(b). To lower the energy of the system, electrons transfer from the pink P2 atom to the dark purple P1 atom. As evidenced in Fig. S4 [36], P1 exhibits a higher Integral Partial Density of States (IPDOS) value compared to P2 at the Fermi level, suggesting more electrons accumulating on P1 than on P2. While in the PE phase, the IPDOS is the same for P1 and P2 because of degeneracy. Meanwhile, the p_x lone pair electrons form on the dark purple P1 atoms, as the extended electron localization function (ELF) on P1 atom [42] and partial charge density of the topmost band plotted in Fig. S5 [36]. This mechanism, regarded as the charge transfers induced symmetry breaking, is important for the polarization. The charge redistribution contributes significantly to the nonlinear electronic component of polarization as shown in Fig. S6 [36], which competes with the linear ionic polarization and results in a nonmonotonic relationship between polarization and distortion amplitude. A similar trend of polarization variation is also observed in α-As6 as plotted in Fig. S3(e)–(f) [36], but the structure has already been in its most stable state before the polarization starts to decrease. Therefore, α-As6 exhibits a significantly larger in-plane polarization of 34.08 pC/m compared to α-P6, despite having a smaller $\Delta\theta$ value. Moreover, since the semilocal functionals may overdelocalized the lone pair electrons [43], we perform HSE06 calculations and the ferroelectricity-related properties shown in the Supplemental Material part V [36]. The nonmonotonicity in the total polarization by HSE06 functionals is more pronounced compared to the LDA one. For instance, the in-plane polarization of α-As6 also becomes nonmonotonic with distortions in Fig. S9 [36]. These results indicate that the HSE06 functionals enhance the localization of lone pair electrons and charge transfer.

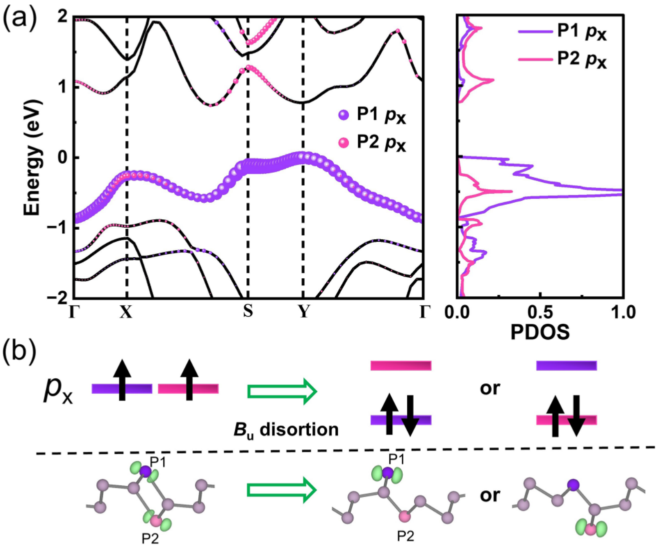

FIG. 2. (a) The projected band structure and density of states of α-P6. (b) The charge transfers induced distortion schematic from PE to FE α-P6. The bottom panel is the partial charges of the valence band at the S point in the Brillouin zone (isosurface of 0.015 e/Bohr^3 and 0.03 e/Bohr^3 for PE and FE, respectively). The dark purple atom and pink atom denote P1 and P2.

Taking advantage of the charge transfer and the special p_x orbitals at the valence band maximum, it is feasible to perform STM characterizations to flip the polarizations as well as distinguish the direction. The STM simulations of FE and FE' phases are shown in Fig. S11 [36]. When the polarization is downward, one can observe the p_x orbitals of P1 atoms, where two lines of light spots will be shown in STM images. In contrast, as the polarization is reversed, only one line of light spots is present besides the original column.

Strain engineering has proven to be a powerful tool in manipulating 2D ferroelectric materials. For instance, strain can drive phase transition between different In_2Se_3 ferroelectric phases [44] or even introduce ferroelectricity in black phosphorene [45]. Upon careful examination of the α-P6 structure, one observes that it shares similarities with blue phosphorene but with strong out-of-plane displacements on two of the atoms, leading to much smaller a lattice. Therefore, it is possible to achieve the ferroelectric α-P6 by applying uniaxial compressive strain on blue phosphorene along a direction that has been fabricated experimentally [46,47]. The strain-phase diagram is constructed in Fig. 3(b) and shows that the α-P6 is a metastable phase compared to blue and black phosphorene without any strain. However, in experiments, some metastable elemental allotropes with relatively high energy have been successfully synthesized through some nonequilibrium growth processes, or grown on certain substrates and boundaries, such as well-known C60 fullerene, biphenylene, pentagonal Si nanoribbons and so on [48–51]. Here, by applying a compressive strain of 6.3%, blue phosphorene may transform into black phosphorene. To achieve the desired polar α-P6 phase, a larger strain of 10% is required. However, the phase diagram only shows the thermal stability and the dynamical process is also important for the phase transition. We further perform CI-NEB calculations to examine the reaction energy at each phase transition point in Fig. 3(c). Although a smaller strain is required, the phase transformation from blue phosphorene to black phosphorene exhibits quite a high energy barrier of 0.49 eV/atom, which is difficult to overcome in the experiment. In contrast, the structural similarity between blue phosphorene and α-P6 is helpful in reducing the barrier considerably, and only ~ 0.11 eV/atom is required. We also confirm that α-P6 will not transform into black phosphorene spontaneously due to the high reaction energy shown in Fig. S13 [36]. It is noted that the experimental fabrication of blue phosphorene is still difficult and that suitable substrates are needed [45,46]. Besides, though there have been practical researches working on inducing strain on 2D materials [52],

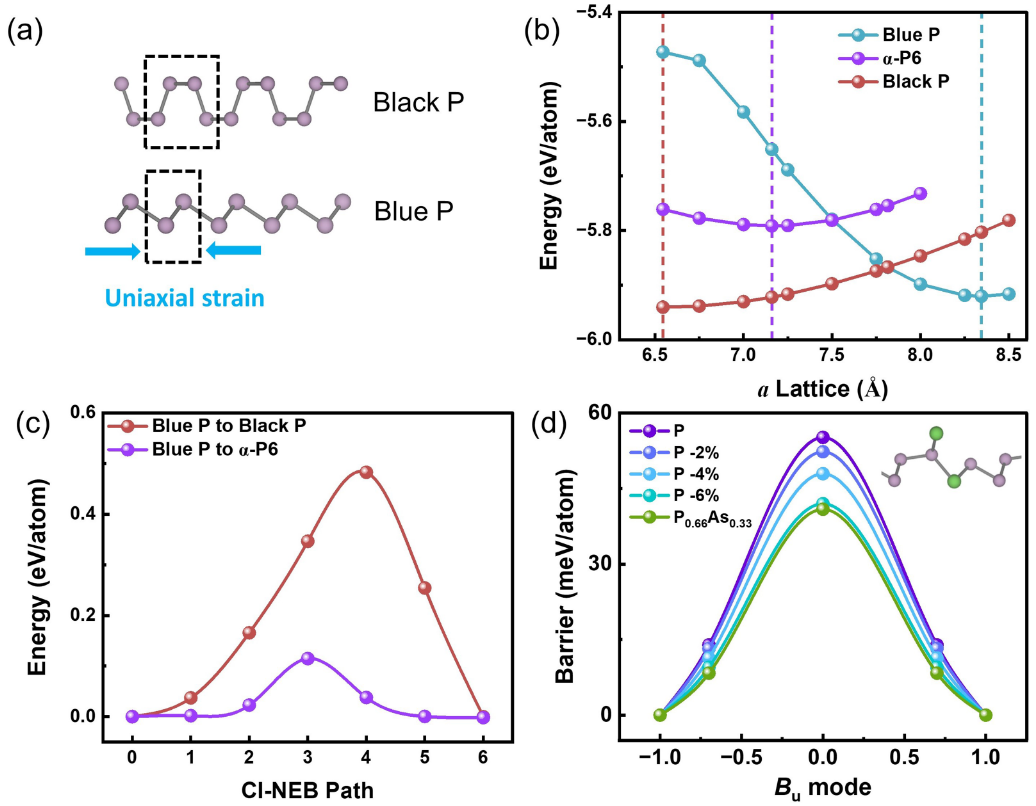

FIG. 3. (a) The geometric structures of monolayer black phosphorene and blue phosphorene. (b) The strain phase diagram of P allotropes. The color line represents the optimized lattice of each allotrope. (c) The energy variation between blue phosphorene and other allotropes at the phase transition points. The CI-NEB path number zero denotes the blue phosphorene, and six denotes black phosphorene and α-P6. (d) Ferroelectric switching energy curve of α-P6 under uniaxial compressive strain and As substitution. The inset is the structure of α-$P_{0.66}As_{0.33}$6, with purple and green atoms corresponding to P and As.

large compressive strain is still challenging and often induces buckling and folding. As a result, we may expect that α-P6 could form under extreme strain conditions, particularly in regions such as buckling boundaries within blue phosphorene, where this polar structure was initially proposed [26].

Meanwhile, as shown in Fig. 3(d), the application of compressive strain on α-P6 facilitates the reduction of the polarization switching barrier, owing to the shorter a lattice of paraelectric structure (depicted in Fig. S3 [36]). Another strategy to achieve switchable polarization is inspired by works that introduce other trivalent ions in wurtzite AlN [53], where the resulting enhancement of ionicity is beneficial for stabilizing the multicoordinated centrosymmetric structure and thus reduces the ferroelectric transition barrier [54,55]. For phosphorous, As substitution has been confirmed feasible in $\alpha - P_{1-x}As_x$ [56]. Therefore, we replace 33% P atoms by As atoms (Fig. S14 [36]) and the most stable structure is shown in the inset of Fig. 3(d). Bader charge analysis shows that the ionicity is indeed increased (Fig. S15 [36]) accompanied by a reduced barrier of 41 meV/atom. These modified polarization switching barriers are comparable to $Cu(CrS_2)_2$ (30 meV/atom, 2 pC/m) [57,58] and the distorted monolayer GaSe (180 meV/atom, 4.89 pC/m) [59], whose ferroelectric polarizations are small but successfully examined by Piezoresponse Force Microscopic (PFM) and utilized in a ferroelectric field effect transistor and other devices. The switchable polarizations of α-P6 enable its applications for next-generation nonvolatile memory.

Ferroelectric materials also exhibit piezoelectric effects, which are useful to generate a change of surface charge in response to external strain. This property renders them invaluable in a wide range of applications including sensors, nanogenerators, catalysis, and other fields [60–62]. Given that 2D materials are stress free in the out-of-plane direction, the piezoelectric stress tensor of α-X6 with Pm space group can be described with five independent components, and the relative parameters obtained by DFPT are listed in the following Table II.

$$e_{ij} = \begin{pmatrix} e_{11} & e_{12} & 0 \\ 0 & 0 & e_{26} \\ e_{31} & e_{32} & 0 \end{pmatrix}.$$

The total piezoelectric stress tensor e_{ij} can be decomposed into clamped-ion term $\bar{e}_{ij}$ and internal-strain term e'_{ij} to distinguish the origins of piezoelectricity [63]. The clamped-ion term $\bar{e}_{ij}$ is obtained by calculating the change of polarization under strain with fixed the atomic positions, which represents the electronic origins. The internal-strain term e'_{ij} stands for ionic contributions, which is defined as the product of Born effective charge $Z^*_{n,ik}$ and the variation of atomic fractional coordination with strain $\frac{\partial u_{n,k}}{\partial \eta_j}$. Here, n is the atomic number

TABLE II. The piezoelectric stress coefficients e_{ij} (pC/m), elastic stiffness modulus C_{jk} (N/m), and piezoelectric strain coefficients d_{ik} (pC/N) of α-X6 (X = P, As).

Structure	e_{11}	e_{31}	e_{12}	e_{32}	e_{26}	C_{11}	C_{12}	C_{22}	C_{66}	d_{11}
α-P6	168.4	1.8	−165.6	−13.4	131.5	37.8	5.8	96.7	13.8	4.8
α-As6	222.7	4.8	−240.8	−3.0	257.8	21.0	7.3	65.0	6.6	11.8

and η_j is the strain. S represents the in-plane area and l_k is the lattice along k direction. Thus, the definition of e_{11} is as following:

$$e_{11} = \bar{e}_{11} + e_{11}^{'} = \bar{e}_{11} + \sum_{n=1}^{6}\sum_{k=1}^{3} \frac{\partial u_{n,k}}{\partial \eta_1} \times \frac{Z_{n,1k}^{*} e l_k}{\mathrm{S}}.$$

We analyze the most relevant longitudinal piezoelectric constant e_{11} of α-X6 with the aforementioned equations. The total e_{11} of α-P6 is dominated by a positive $\bar{e}_{11}$ of 235 pC/m [Fig. 4(a)], while the negative ionic contribution $e_{11}^{'} = -33$pC/m is quite small, which is close to the DFPT results. The small $e_{11}^{'}$ can be attributed to the opposite contributions along the x and z directions, which cancel out each other as shown in Fig. 4(b). The total e_{11} of α-P6 is 202 pC/m, larger than 2D honeycomb compounds GaSe (147 pC/m) and h-BN (138 pC/m) [64].

Finally, since it is the piezoelectric-stress tensor d_{ik} that can be directly characterized by PFM, we introduce the stress-strain tensor C_{jk} for converting e_{ij} to d_{ik}:

$$d_{ik} = \sum_{k=1}^{3} e_{ij} C_{jk}^{-1}.$$

The piezoelectric strain constant d_{11} of α-P6 is 4.8 pC/N, while α-As6 exhibits a larger d_{11} value of 11.8 pC/N. This enhanced piezoelectric response in α-As6 can be attributed to both a larger e_{11} as well as smaller elastic stiffness modulus as in Table II. Notably, even though α-X6 have a smaller e_{11} than MoS_2 ($e_{11} = 364$ pC/m, $d_{11} = 3.73$ pC/N), their d_{11} is larger. This is attributed to the higher flexibility of α-X6 structure compared to MoS_2 [65]. As a result, taking advantage of the moderate piezoelectric strain constants and flexible structure, α-X6 emerges as a potential candidate for efficient energy harvesting and conversion devices.

IV. CONCLUSION

In conclusion, α-X6 (X = P, As) is a novel elemental ferroelectric material exhibiting coupled in-plane and out-of-plane polarization. Charge transfer and the formation of p_x lone pair electrons contribute significantly to its elemental polarization. Compressive strain may facilitate a phase transformation from blue phosphorene to the metastable α-P6 phase, since the equilibrium transition to black phosphorene is kinetically suppressed. In addition, strain and substitution can reduce the energy barrier for polarization switching for practical ferroelectric utilizations. Moreover, the moderate e_{11} and flexible characters result in the high longitudinal piezoelectric coefficient d_{11} in α-X6, making it suitable for energy-mechanical conversion applications. Our findings enrich the family of elemental ferroelectrics and hold great promise for elemental ferroelectrics and piezoelectric applications.

ACKNOWLEDGMENTS

This work was financially supported by the National Key R&D Program of China (2019YFE0112000), the Zhejiang Provincial Natural Science Foundation of China (LR21A040001, LDT23F04014F01), and the National Natural Science Foundation of China (No. 11974307).

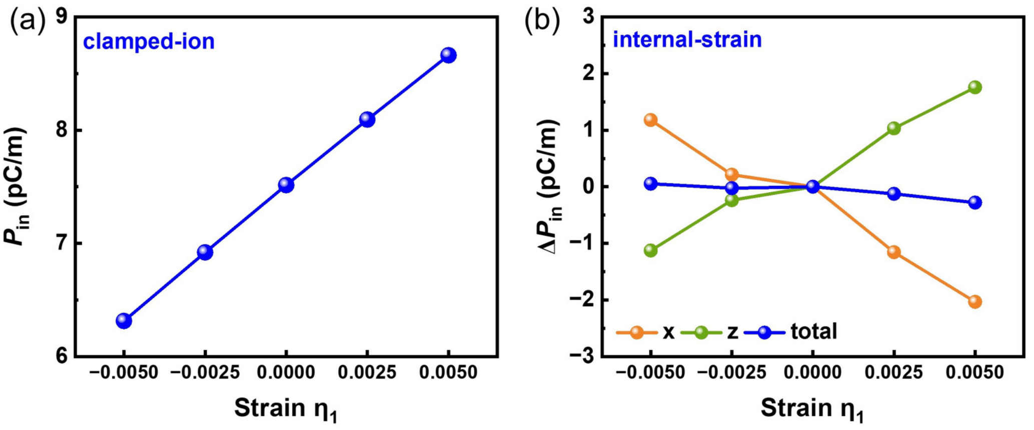

FIG. 4. The polarization-strain variation of α-P6 decomposed into (a) clamped-ion and (b) internal-strain term.

[1] C. Xiao, F. Wang, S. A. Yang, Y. Lu, Y. Feng, and S. Zhang, Elemental ferroelectricity and antiferroelectricity in group-V monolayer, Adv. Funct. Mater. **28**, 1707383 (2018).

[2] J. Gou, H. Bai, X. Zhang, Y. L. Huang, S. Duan, A. Ariando, S. A. Yang, L. Chen, Y. Lu, and A. T. S. Wee, Two-dimensional ferroelectricity in a single-element bismuth monolayer, Nature (London) **617**, 67 (2023).

[3] Y. Guo, C. Zhang, J. Zhou, Q. Wang, and P. Jena, Lattice dynamic and instability in pentasilicene: A light single-element ferroelectric material with high curie temperature, Phys. Rev. Appl. **11**, 064063 (2019).

[4] C. Xiao, X. Wang, X. Pi, S. A. Yang, Y. Feng, Y. Lu, and S. Zhang, Spontaneous symmetry lowering of Si (001) towards two-dimensional ferro/antiferroelectric behavior, Phys. Rev. Mater. **3**, 044410 (2019).

[5] D. Liu, L. Han, R. Wei, S. Song, J. Guan, S. Dong, and D. Tománek, Unusual electric polarization behavior in elemental quasi-two-dimensional allotropes of selenium, Phys. Rev. Mater. **6**, 103403 (2022).

[6] Y. Wang, C. Xiao, M. Chen, C. Hua, J. Zou, C. Wu, J. Jiang, S. A. Yang, Y. Lu, and W. Ji, Two-dimensional ferroelectricity and switchable spin-textures in ultra-thin elemental Te multilayers, Mater Horiz **5**, 521 (2018).

[7] L. Yang, S. Ding, J. Gao, and M. Wu, Atypical sliding and moire ferroelectricity in pure multilayer graphene, Phys. Rev. Lett. **131**, 096801 (2023).

[8] A. Garcia-Ruiz, V. Enaldiev, A. McEllistrim, and V. I. Fal'Ko, Mixed-stacking few-layer graphene as an elemental weak ferroelectric material, Nano Lett. **23**, 4120 (2023).

[9] Y. Liang, R. Guo, S. Shen, B. Huang, Y. Dai, and Y. Ma, Out-of-plane ferroelectricity and multiferroicity in elemental bilayer phosphorene, arsenene, and antimonene, Appl. Phys. Lett. **118**, 12905 (2021).

[10] N. R. Alluri, N. P. Maria Joseph Raj, G. Khandelwal, P. K. Panda, A. Banerjee, Y. K. Mishra, R. Ahuja, and S. Kim, Crystallinity modulation originates ferroelectricity like nature in piezoelectric selenium, Nano Energy **95**, 107008 (2022).

[11] G. Rao, H. Fang, T. Zhou, C. Zhao, N. Shang, J. Huang, Y. Liu, X. Du, P. Li, X. Jian, L. Ma, J. Wang, K. Liu, J. Wu, X. Wang, and J. Xiong, Robust piezoelectricity with spontaneous polarization in monolayer tellurene and multilayer tellurium film at room temperature for reliable memory, Adv. Mater. **34**, 2204697 (2022).

[12] S. Zhong, X. Zhang, S. Liu, S. A. Yang, and Y. Lu, Giant and nonanalytic negative piezoelectric response in elemental group-Va ferroelectric monolayers, Phys. Rev. Lett. **131**, 236801 (2023).

[13] Z. Wang and S. Dong, Large in-plane negative piezoelectricity and giant nonlinear optical susceptibility in elementary ferroelectric monolayers, Phys. Rev. B **108**, 235423 (2023).

[14] Y. Guo, H. Zhu, and Q. Wang, Large second harmonic generation in elemental $\alpha-\text{Sb}$ and $\alpha-\text{Bi}$ monolayers, J. Phys. Chem. C **124**, 5506 (2020).

[15] Z. Qian, J. Zhou, H. Wang, and S. Liu, Shift current response in elemental two-dimensional ferroelectrics, npj Comput. Mater. **9**, 67 (2023).

[16] Y. Wang, S. Sun, J. Zhang, Y. L. Huang, and W. Chen, Recent progress in epitaxial growth of two-dimensional phosphorus, Smartmat **2**, 286 (2021).

[17] S. Nahas, A. Bajaj, and S. Bhowmick, Polymorphs of two dimensional phosphorus and arsenic: Insight from an evolutionary search, Phys. Chem. Chem. Phys. **19**, 11282 (2017).

[18] G. Schusteritsch, M. Uhrin, and C. J. Pickard, Single-layered hittorf's phosphorus: A wide-bandgap high mobility 2d material, Nano Lett. **16**, 2975 (2016).

[19] M. Wu, H. Fu, L. Zhou, K. Yao, and X. C. Zeng, Nine new phosphorene polymorphs with non-honeycomb structures: A much extended family, Nano Lett. **15**, 3557 (2015).

[20] P. G. Demingos and A. R. Muniz, Prediction of $\phi-\text{p}$ and $\sigma-\text{P}$: Two new strain-interconvertible phosphorene allotropes, J. Phys. Chem. C **124**, 21207 (2020).

[21] M. Ruck, D. Hoppe, B. Wahl, P. Simon, Y. Wang, and G. Seifert, Fibrous red phosphorus, Angew. Chem. Int. Ed. **44**, 7616 (2005).

[22] L. Zhang, H. Huang, B. Zhang, M. Gu, D. Zhao, X. Zhao, L. Li, J. Zhou, K. Wu, Y. Cheng, and J. Zhang, Structure and properties of violet phosphorus and its phosphorene exfoliation, Angew. Chem. **132**, 1090 (2020).

[23] Z. Zhu and D. Tománek, Semiconducting layered blue phosphorus: A computational study, Phys. Rev. Lett. **112**, 176802 (2014).

[24] L. Li, Y. Yu, G. J. Ye, Q. Ge, X. Ou, H. Wu, D. Feng, X. H. Chen, and Y. Zhang, Black phosphorus field-effect transistors, Nat. Nanotechnol. **9**, 372 (2014).

[25] Y. Kaddar, W. Zhang, H. Enriquez, Y. J. Dappe, A. Bendounan, G. Dujardin, O. Mounkachi, A. El Kenz, A. Benyoussef, A. Kara, and H. Oughaddou, Dirac fermions in blue phosphorene monolayer, Adv. Funct. Mater. **33**, 2213664 (2023).

[26] J. Liu, Y. Guo, S. Zhang, Q. Wang, Y. Kawazoe, and P. Jena, New phosphorene allotropes containing ridges with 2- and $4-$ coordination, J. Phys. Chem. C **119**, 24674 (2015).

[27] G. Kresse and J. Furthmüller, Efficient iterative schemes for ab initio total-energy calculations using a plane-wave basis set, Phys. Rev. B **54**, 11169 (1996).

[28] J. P. Perdew and A. Zunger, Self-interaction correction to density functional approximations for many wlectrons systems, Phys. Rev. B **23**, 5048 (1981).

[29] P. E. Blöchl, Projector augmented-wave method, Phys. Rev. B **50**, 17953 (1994).

[30] A. V. Krukau, O. A. Vydrov, A. F. Izmaylov, and G. E. Scuseria, Influence of the exchange screening parameter on the performance of screened hybrid functionals, J. Chem. Phys. **125**, 224106 (2006).

[31] R. D. King-Smith and D. Vanderbilt, Theory of polarization of crystalline solids, Phys. Rev. B **47**, 1651 (1993).

[32] X. Wu, D. Vanderbilt, and D. R. Hamann, Systematic treatment of displacements, strains, and electric fields in density-functional perturbation theory, Phys. Rev. B **72**, 035105 (2005).

[33] G. Henkelman, B. P. Uberuaga, and H. Jónsson, A climbing image nudged elastic band method for finding saddle points and minimum energy paths, J. Chem. Phys. **113**, 9901 (2000).

[34] V. Wang, N. Xu, J. Liu, G. Tang, and W. Geng, VASPKIT: A user-friendly interface facilitating high-throughput computing and analysis using VASP code, Comput. Phys. Commun. **267**, 108033 (2021).

[35] P. A. Fleury, J. F. Scott, and J. M. Worlock, Soft phonon modes and 110 degrees K phase transition in SrTiO_3, Phys. Rev. Lett. **21**, 16 (1968).

[36] See Supplemental Material at http://link.aps.org/supplemental/10.1103/PhysRevMaterials.8.084401 for the phonon spectrum of ferroelectric α-P6; the CI-NEB energy of polarization reversal; the ferroelectric properties of α-As6; the IPDOS, ELF, electronic and ionic polarization; HSE06 functionals results; STM simulation images; energy-lattice curve and transformation energy of α-P6; the relative energy and Bader charge analysis of $\alpha-\mathrm{P}_{0.66}\mathrm{As}_{0.33}6$; the piezoelectric related properties of α-X6.

[37] L. Li and M. Wu, Binary compound bilayer and multilayer with vertical polarizations: Two-dimensional ferroelectrics, multiferroics, and nanogenerators, ACS Nano **11**, 6382 (2017).

[38] Z. Zheng, Q. Ma, Z. Bi, S. de la Barrera, M. H. Liu, N. Mao, Y. Zhang, N. Kiper, K. Watanabe, T. Taniguchi, J. Kong, W. A. Tisdale, R. Ashoori, N. Gedik, L. Fu, S. Y. Xu, and P. Jarillo-Herrero, Unconventional ferroelectricity in moire heterostructures, Nature (London) **588**, 71 (2020).

[39] S. M. Vizner, Y. Waschitz, W. Cao, I. Nevo, K. Watanabe, T. Taniguchi, E. Sela, M. Urbakh, O. Hod, and S. M. Ben, Interfacial ferroelectricity by van der waals sliding, Science **372**, 1462 (2021).

[40] K. Yasuda, X. Wang, K. Watanabe, T. Taniguchi, and P. Jarillo-Herrero, Stacking-engineered ferroelectricity in bilayer boron nitride, Science **372**, 1458 (2021).

[41] A. Chanana and U. V. Waghmare, Prediction of coupled electronic and phononic ferroelectricity in strained 2D h-NbN: First-principles theoretical analysis, Phys. Rev. Lett. **123**, 037601 (2019).

[42] A. D. Becke and K. E. Edgecombe, A simple measure of electron localization in atomic and molecular systems, J. Chem. Phys. **92**, 5397 (1990).

[43] M. W. Swift and J. L. Lyons, Lone-pair stereochemistry induces ferroelectric distortion and the rashba effect in inorganic halide perovskites, Chem. Mater. **35**, 9370 (2023).

[44] W. Han, X. Zheng, K. Yang, C. S. Tsang, F. Zheng, L. W. Wong, K. H. Lai, T. Yang, Q. Wei, M. Li, W. F. Io, F. Guo, Y. Cai, N. Wang, J. Hao, S. P. Lau, C. Lee, T. H. Ly, M. Yang, and J. Zhao, Phase-controllable large-area two-dimensional $\mathrm{In_2Se_3}$ and ferroelectric heterophase junction, Nat. Nanotechnol. **18**, 55 (2023).

[45] W. Xu, J. D. Zheng, W. Y. Tong, J. L. Wang, Y. P. Shao, Y. K. Zhang, Y. F. Tan, and C. G. Duan, Strain-induced ferroelectric phase transition in group-V monolayer black phosphorus, Adv. Quantum Technol. **6**, 2200169 (2023).

[46] J. L. Zhang, S. Zhao, S. Sun, H. Ding, J. Hu, Y. Li, Q. Xu, X. Yu, M. Telychko, J. Su, C. Gu, Y. Zheng, X. Lian, Z. Ma, R. Guo, J. Lu, Z. Sun, J. Zhu, Z. Li, and W. Chen, Synthesis of monolayer blue phosphorus enabled by silicon intercalation, ACS Nano **14**, 3687 (2020).

[47] S. Yang, Z. Hu, W. Wang, P. Cheng, L. Chen, and K. Wu, Regular arrangement of two-dimensional clusters of blue phosphorene on Ag(111), Chinese Phys. Lett. **37**, 96803 (2020).

[48] W. Krätschmer, L. D. Lamb, K. Fostiropoulos, and D. R. Huffman, Solid C60: A new form of carbon, Nature (London) **347**, 354 (1990).

[49] Q. Fan, L. Yan, M. W. Tripp, O. Krejčí, S. Dimosthenous, S. R. Kachel, M. Chen, A. S. Foster, U. Koert, P. Liljeroth, and J. M. Gottfried, Biphenylene network: A nonbenzenoid carbon allotrope, Science **372**, 852 (2021).

[50] S. Sheng, R. Ma, J. Wu, W. Li, L. Kong, X. Cong, D. Cao, W. Hu, J. Gou, J. Luo, P. Cheng, P. Tan, Y. Jiang, L. Chen, and K. Wu, The pentagonal nature of self-assembled silicon chains and magic clusters on Ag(110), Nano Lett. **18**, 2937 (2018).

[51] P. Y. Huang, C. S. Ruiz-Vargas, A. M. van der Zande, W. S. Whitney, M. P. Levendorf, J. W. Kevek, S. Garg, J. S. Alden, C. J. Hustedt, Y. Zhu, J. Park, P. L. McEuen, and D. A. Muller, Grains and grain boundaries in single-layer graphene atomic patchwork quilts, Nature (London) **469**, 389 (2011).

[52] S. Yang, Y. Chen, and C. Jiang, Strain engineering of two-dimensional materials: Methods, properties, and applications, Infomat **3**, 397 (2021).

[53] V. S. Calderon, J. Hayden, S. M. Baksa, W. Tzou, S. Trolier-McKinstry, I. Dabo, J. P. Maria, and E. C. Dickey, Atomic-scale polarization switching in wurtzite ferroelectrics, Science **380**, 1034 (2023).

[54] T. T. Zhong, Y. Gao, Y. Ren, and M. Wu, Theoretical designs of low-barrier ferroelectricity, Wires Computational Molecular Science **13**, e1682 (2023).

[55] Z. Liu, X. Wang, X. Ma, Y. Yang, and D. Wu, Doping effects on the ferroelectric properties of wurtzite nitrides, Appl. Phys. Lett. **122**, 122901 (2023).

[56] Z. Zhu, J. Guan, and D. Tománek, Structural transition in layered $\mathrm{As}_{1-x}\mathrm{P}_x$ compounds: A computational study, Nano Lett. **15**, 6042 (2015).

[57] T. Zhong, X. Li, M. Wu, and J. Liu, Room-temperature multiferroicity and diversified magnetoelectric couplings in 2D materials, Natl. Sci. Rev. **7**, 373 (2020).

[58] X. Xu, T. Zhong, N. Zuo, Z. Li, D. Li, L. Pi, P. Chen, M. Wu, T. Zhai, and X. Zhou, High-Tc two-dimensional ferroelectric CuCrS(2) grown via chemical vapor deposition, ACS Nano **16**, 8141 (2022).

[59] W. Li, X. Zhang, J. Yang, S. Zhou, C. Song, P. Cheng, Y. Zhang, B. Feng, Z. Wang, Y. Lu, K. Wu, and L. Chen, Emergence of ferroelectricity in a nonferroelectric monolayer, Nat. Commun. **14**, 2757 (2023).

[60] X. Jiang, K. Kim, S. Zhang, J. Johnson, and G. Salazar, High-temperature piezoelectric sensing, Sensors-Basel **14**, 144 (2014).

[61] D. Zhang, D. Wang, Z. Xu, X. Zhang, Y. Yang, J. Guo, B. Zhang, and W. Zhao, Diversiform sensors and sensing systems driven by triboelectric and piezoelectric nanogenerators, Coordin. Chem. Rev. **427**, 213597 (2021).

[62] S. Tu, Y. Guo, Y. Zhang, C. Hu, T. Zhang, T. Ma, and H. Huang, Piezocatalysis and piezo-photocatalysis: Catalysts classification and modification strategy, reaction mechanism, and practical application, Adv. Funct. Mater. **30**, 2005158 (2020).

[63] G. Saghi-Szabo, R. E. Cohen, and H. Krakauer, First-principles study of piezoelectricity in $\mathrm{PbTiO_3}$, Phys. Rev. Lett. **80**, 4321 (1998).

[64] W. Li and J. Li, Piezoelectricity in two-dimensional group-III monochalcogenides, Nano Res. **8**, 3796 (2015).

[65] M. N. Blonsky, H. L. Zhuang, A. K. Singh, and R. G. Hennig, Ab initio prediction of piezoelectricity in two-dimensional materials, ACS Nano **9**, 9885 (2015).